BIOCHEMISTRY
including biophysical chemistry & molecular biology

Article

pubs.acs.org/biochemistry

Mechanism of Benzylic Hydroxylation by 4-Hydroxymandelate Synthase. A Computational Study

Anna Wójcik,[†] Ewa Broclawik,[†] Per E. M. Siegbahn,[‡] and Tomasz Borowski*[,†]

[†]Jerzy Haber Institute of Catalysis and Surface Chemistry, Polish Academy of Sciences, ul. Niezapominajek 8, 30-239 Cracow, Poland

[‡]Department of Physics, Stockholm Center for Physics, Astronomy and Biotechnology, Stockholm University, S-106 91 Stockholm, Sweden

Supporting Information

ABSTRACT: Hydroxymandelate synthase (HMS) and 4-hydroxyphenylpyruvate dioxygenase (HPPD) are highly related enzymes using the same substrates but catalyzing hydroxylation reactions yielding different products. The first steps of the HMS and HPPD catalytic reactions are believed to proceed in the same way and lead to an Fe(IV)═O−hydroxyphenylacetate (HPA) intermediate. Further down the catalytic cycles, HMS uses Fe(IV)═O to perform hydroxylation of the benzylic carbon, whereas in HPPD, the reactive oxoferryl intermediate attacks the aromatic ring of HPA. This study focuses on this part of the HMS catalytic cycle that starts from the oxoferryl intermediate and aims to identify interactions within the active site that are responsible for enzyme specificity. To this end, a HMS−Fe(IV)═O−HPA complex was modeled with molecular dynamics simulations. On the basis of the molecular dynamics-equilibrated structure, an active site model suitable for quantum chemical investigations was constructed and used for density functional theory (B3LYP) calculations of the mechanism of the native reaction of HMS, i.e., benzylic hydroxylation, and the alternative electrophilic attack on the ring, which is a step of the HPPD catalytic cycle. The most important result of this study is the finding that the conformation of the Ser201 side chain in the second coordination shell has a key role in directing the reaction of Fe(IV)═O into either the HMS or the HPPD channel.

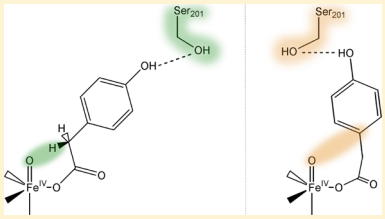

4-Hydroxymandelate synthase (HMS) and 4-hydroxyphenylpyruvate dioxygenase (HPPD) are closely related enzymes that belong to the superfamily of Fe(II) and α-keto acid-dependent dioxygenases. They constitute a subgroup within this large α-keto acid-dependent superfamily, in which the organic substrate, i.e., 4-hydroxyphenylpyruvate [HPP (Figure 1)],

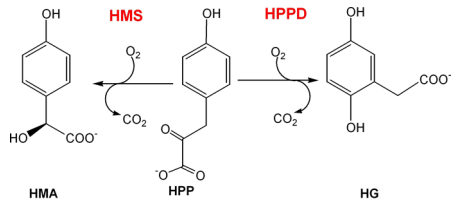

Figure 1. Reactions catalyzed by HMS and HPPD.

includes a keto acid functional group. Therefore, HMS and HPPD do not require α-ketoglutarate (α-KG), which is a necessary cosubstrate for the majority of the α-keto acid-dependent dioxygenases.

HMS was found in certain strains of bacteria and was shown to catalyze the first step in the conversion of HPP to *p*-hydroxyphenylglycine, which is a building block of several macrocyclic nonribosomal peptide antibiotics, e.g., vancomycin.[1] The reaction catalyzed by HMS is a transformation of HPP to (*S*)-4-hydroxymandelate (HMA), which means decarboxylation and hydroxylation of the aliphatic part of the substrate (Figure 1). HPPD converts HPP to 2,5-dihydroxyphenylacetate [homogentisate (HG)], which implies decarboxylation and then migration of the aliphatic side chain instigated by hydroxylation of the aromatic ring. This reaction is a second step of tyrosine catabolism eventually leading to acetoacetate and fumarate.[2]

With regard to the overall structure of the enzymes, it is based on two barrel-like domains with $\beta\alpha\beta\beta\beta\alpha$ topology and is similar to that found in extradiol dioxygenases.[3,4] The latter suggests that HPPD, HMS, and extradiol dioxygenases are evolutionarily related. In terms of chemistry of the catalytic reaction, HPPD and HMS coincide with α-ketoglutarate-dependent enzymes, whose structural motif is a double-stranded β-helix (jellyroll).[3,4] HMS and HPPD have the same overall tertiary structure and are characterized by a highly identical (~34%) and similar (~43%) sequences.[5]

The active sites of HMS and HPPD are formed from residues of the C-terminal half of the protein, whereas the function of the N-terminal part is currently unknown. The substrate binding cavity is considerably smaller in HMS (30 Å^3) than in HPPD (63 Å^3).[5] In the available crystal structure of HMS complexed with its product and cobalt instead of iron [Protein Data Bank (PDB) entry 2R5V (Figure 2)], it can be observed that HMA coordinates the metal ion in a bidentate fashion through one of the carboxylate oxygens and the oxygen

Received: August 14, 2012
Revised: October 31, 2012
Published: November 5, 2012

   dx.doi.org/10.1021/bi3010957 | *Biochemistry* 2012, 51, 9570−9580

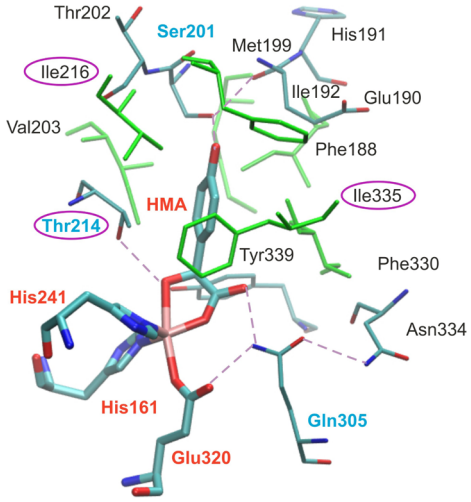

Figure 2. Active site region of the X-ray structure of the HMS–Co(II)–HMA complex (PDB entry 2R5V). First-shell ligands in ball-and-stick representation (residue names colored red), residues forming hydrogen bonds with the first-shell ligands in dark colors (residue names colored blue), and labels of residues substituted in mutation studies shown as violet ovals. Hydrophobic residues are colored green.

of the benzylic hydroxyl group. Two histidine ligands (His161 and His241) and the carboxylate group of HMA define the equatorial plane, whereas a glutamate (Glu320) and the hydroxyl group of HMA are in axial positions of a distorted trigonal coordination bipyramid.[5] Besides the direct bond to cobalt, the orientation of HMA within the active site is fixed by hydrogen bonds to three amino acids. Ser201 forms a hydrogen bond with the *p*-hydroxyl group of HMA; Thr214 is involved in a hydrogen bond with the benzylic hydroxyl, and the third interaction is present between Gln305 and one of the oxygens from the carboxylic group of HMA. There are also several van der Waals contacts with the aromatic ring of HMA. For example, Phe188, Thr214, Ile216, and Ile335 are unique to HMS, forming a pocket for the hydrophobic part of the substrate (Figure 2).[5] Their counterparts in HPPD are Arg188, Pro214, Asn216, and Phe337.

Experimental spectroscopies employing a combination of circular dichroism (CD), magnetic circular dichroism (MCD), and variable-temperature, variable-field (VTVH) MCD have been used to gain insight into structures of active sites in the resting form of HPPD and its complex with the substrate.[6] These experiments revealed that in the resting form of HPPD the metal cofactor is mainly six-coordinate (6C) with a small amount of a five-coordinate (5C) component, and the HPPD–Fe(II)–HPP complex is a similar mixture of 5C and 6C forms with the substrate bound to Fe(II) in a bidentate fashion.[6] Moreover, in the MCD studies, a spectral feature was observed showing opposite signs for the enzyme–substrate complexes of HMS and HPPD, which was attributed to different arrangements of the aromatic ring of the substrate in the active sites of the two enzymes.[6]

The reaction of the 5C complex with O_2 has been studied with density functional theory (DFT) methods, and it was suggested that after dioxygen binding a nucleophilic attack of the bound dioxygen on the carbonyl carbon of HPP elicits decarboxylation and leads, through a peracid intermediate, to a complex with 4-hydroxyphenylacetate (HPA) and the Fe(IV)=O moiety (Figure 3).[7] This species is the last common intermediate in the catalytic cycles of HMS and HPPD, and at

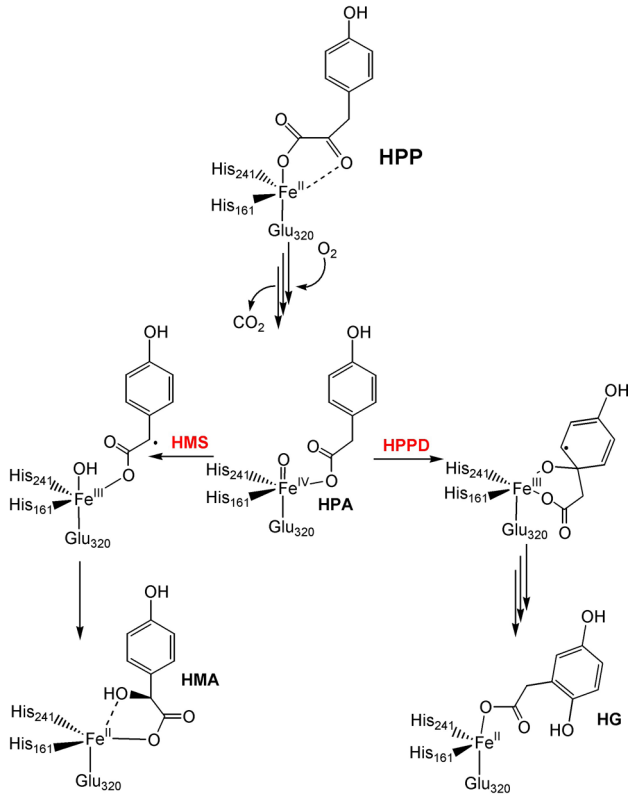

Figure 3. General reaction mechanisms of HMS and HPPD. The residue numbers are for HMS.

this point, the reaction paths of HMS and HPPD diverge. Indeed, in a recent study by Shah et al., wild-type (WT) HPPD and some point mutants of HMS were shown to produce HPA as a side product.[8] Moreover, this type of oxoferryl species has been trapped and characterized by various spectroscopic methods in studies of TauD, another α-keto acid-dependent oxygenase.[9]

The benzylic hydroxylation reaction of HMS was studied with DFT methods by Borowski et al. and later by Neidig et al.[6,7] In both studies, it was found that abstraction of a hydrogen atom from the benzylic position of HPA leads to an intermediate-spin (IS) Fe(III)–OH species, which is in contrast to the usually observed high-spin form. Neidig et al. put forth a convincing explanation for this fact in the language of frontier molecular orbitals.[6] More specifically, the high-spin Fe(IV)=O intermediate has two possible channels for electrophilic reactions: the usually preferred vertical channel, where the reactant approaches the Fe=O unit along the Fe–O bond vector, involving the Fe(IV)=O σ^* orbital (α LUMO) and leading to a high-spin Fe(III)–OH species, and the horizontal channel, where the reactant approaches the Fe=O unit perpendicular to the Fe–O bond vector, involving the π^* Fe(IV)=O orbital (β LUMO) playing an active role, and ends up in the intermediate-spin Fe(III)–OH species. In HMS, the substrate is tethered to the Fe ion, and therefore, the benzylic CH group can approach the oxo ligand only in the horizontal orientation. Hence, the horizontal (π^*) channel is used in this case.[6]

The similarity of HMS and HPPD in terms of sequence and structure encouraged mutation studies that aimed to identify the amino acids decisive for the reaction regioselectivity.[8,10,11] Several attempts were made to switch the reaction specificity

dx.doi.org/10.1021/bi3010957 | *Biochemistry* 2012, 51, 9570–9580

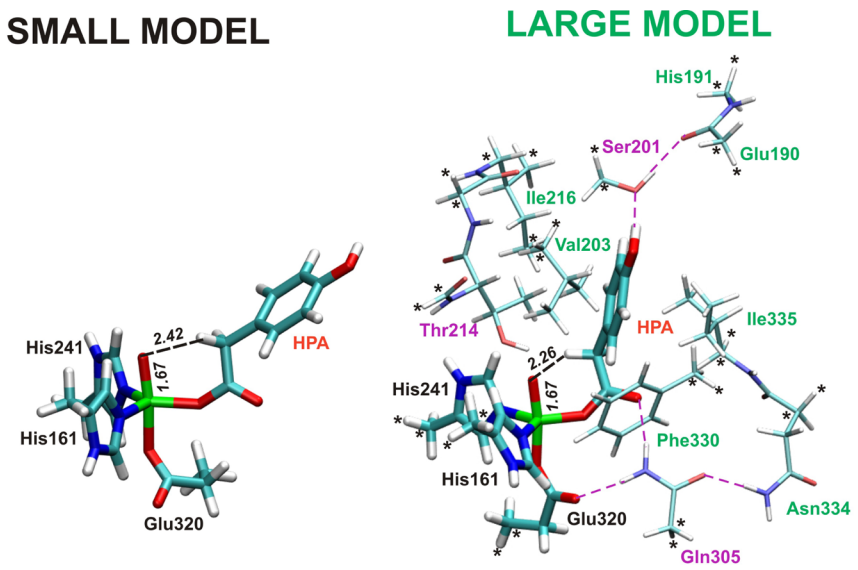

Figure 4. Optimized structures of ^{5}R for the small and large models employed in the quantum mechanics calculations. Atoms marked with asterisks were constrained during the optimizations. Names of residues forming hydrogen bonds with the first-shell ligands are colored violet.

between HMS and HPPD, but they were only partly successful. HMS was shown to be very tolerant to mutations, and all attempts to force HMS to produce HG were unsuccessful. On the other hand, several mutants of HPPD producing HMA along with HG were obtained with directed mutagenesis focused on three residues: Pro214, Asn216, and Phe337.[11] Only two single-point HPPD mutants, i.e., N216I and F337I, were found to produce HMA among other products, including HG, yet a relatively large group of constructs with double mutations yielded product mixtures with greater concentrations of HMA then HG.[10,11] Interestingly, it was shown that a single mutation of Ser201 to alanine has a rather modest effect on the reaction specificity of HMS, whereas for HPPD, this effect is very pronounced.[8]

From the literature survey presented above, it follows that the basics of the catalytic reactions of HMS and HPPD are relatively well understood, but the factors responsible for the reaction specificity remain obscure. In this work, a series of classical molecular dynamics simulations and quantum chemical studies aimed to identify the structural features responsible for directing the HMS reaction into its native channel. As discussed in detail below, the conformation of the second-shell Ser201 side chain is of key importance in this context.

MODELS AND METHODS

Model Setup for Molecular Dynamics. The starting point for constructing a macromolecular model was a crystal structure determined for Co-substituted HMS complexed with the reaction product, i.e., HMA (PDB entry 2R5V),[5] which was prepared for molecular dynamics (MD) simulations in the following way.

First, residues missing in the X-ray structure (Met1 and the Ser107-Glu108-Ala109 loop) were added with Modeller.[12−15] Second, the cobalt ion was substituted with the oxoferryl group, and the final product, i.e., HMA, was replaced with hydroxyphenylacetate (HPA). The protonation states (pH 7.0) of acidic and basic residues, including histidine residues not involved in metal binding, were chosen on the basis of pK_a calculations conducted with the PROPKA server.[16,17] Placement of protons in histidine side chains was checked by the visual inspection of the immediate surrounding of a given histidine in the crystal structure (His40 and His283 were doubly protonated; His62, His106, His124, His149, His234, His299, and His315 were protonated on Nδ; His191 and His213 were protonated on Nε). The total charge of the system obtained in this way is −21 and was therefore compensated with 21 Na^+ ions.

Missing force field parameters for the oxoferryl form of the iron cofactor were derived as follows. First, a model of Fe(IV) with its first coordination shell was fully optimized at the B3LYP/lacvp level. The optimized geometry provided reference values for bond lengths and valence angles, whereas the corresponding force constants were obtained from the Hessian matrix.[18,19] Atomic charges were obtained with the RESP procedure[20] using the electrostatic potential computed at the B3LYP/lacvp/IEFPCM (ε = 4.0) level of theory. The van der Waals parameters for the ferryl ion were taken from the UFF force field.[21] The standard protein residues were described with the FF03 Amber force field.[22] The structure was solvated with TIP3P water[23] in a cuboid with at least 10 Å of water around every solute atom.

Molecular Dynamics Simulations. Prior to the molecular dynamics simulations, the structure of the system was minimized in three steps. First, the water and sodium ions were minimized while the coordinates of the protein and HPA were restrained with a 500 kcal mol^{-1} Å^{-2} harmonic potential. In the second minimization, the restraints were loosened to 10 kcal mol^{-1} Å^{-2}, whereas in the final minimization run, there were no restraints at all. Each minimization run consisted of 500 steps of steepest descent and 4500 steps done with the conjugate gradient algorithm. The minimized structure was heated from 0 to 300 K over a 100 ps long dynamics under constant-volume conditions. In the following step, the structure was subjected to 100 ps long constant-pressure dynamics, which allowed the density of the system to equilibrate. While the sample was heated and its density equilibrated, the coordinates of the protein were restrained with a force constant of 1 kcal mol^{-1} Å^{-2}. The production molecular dynamics simulation was 10 ns long. If not stated otherwise, all molecular dynamics simulations were conducted with a 2 fs time step,

dx.doi.org/10.1021/bi3010957 | Biochemistry 2012, 51, 9570−9580

employing the SHAKE algorithm to constrain covalent bonds of hydrogen atoms, at a constant temperature (300 K) and constant pressure (1 atm) maintained with Langevin dynamics, under periodic boundary conditions. The particle mesh Ewald method was used for electrostatics. Molecular dynamics simulations were performed with Amber 11.[24]

Quantum Chemistry Models and Methods. Two active site models were employed in this work for the quantum chemical computations. The small model included the metal ion and its first coordination shell, and it was constructed on the basis of the crystal structure (PDB entry 2R5V). The large model was based on a structure equilibrated with molecular dynamics simulations, and it included, besides the metal and its first-shell ligands, residues lining the substrate pocket.

In the small model, the cobalt ion and the hydroxymandelate product, both present in the X-ray structure, were replaced with the oxoferryl species and the HPA intermediate, respectively. The amino acids coordinating the iron were modeled by methylimidazoles (His161 and His241) and propionate [Glu320 (see Figure 4)]. In the small model, no constraints were imposed on the atomic coordinates. Compared to the model used in one of the previous studies,[6] the small model differs in the position of the substrate. More specifically, in ref 6 HPA was bound *trans* to glutamate (Glu349, PDB entry 1T47), whereas in this study (and also previously[7]), it is bound in the equatorial plane defined by iron and two histidine ligands, which is an arrangement consistent with the X-ray structure of the HMS−product complex.[5]

Transition states and intermediates are labeled with a generic $^{n}X_{m}$ symbol, where n indicates the multiplicity, X is either R (reactant), INT (intermediate), TS (transition state), MECP (minimum energy crossing point), or P (product) and, if needed, a consecutive number of such species, and m is a symbol of the model (L for large and S for small). In the large model, the first coordination shell was supplemented with fragments of second-shell residues forming the substrate pocket: Ser201, Thr214, and Gln305, which form hydrogen bonds with the iron ligands; Val203, Ile216, Phe330, Asn334, and Ile335, which make van der Waals contacts with HPA; and the Glu190−His191 fragment of the main chain, which forms a hydrogen bond with Ser201. Initial coordinates of the large model were taken from an averaged protein structure computed for the last nanosecond of the MD simulation. Thus, instead of using a particular snapshot from the MD simulation, or minimized structure thereof, averaged coordinates of one thousand snapshots from the last simulated nanosecond were used, which can be viewed as an analogy to the crystal structure, which is a time and space average. Constraints were imposed on atomic coordinates of hydrogen and carbon atoms corresponding to Cα and Cβ in His161, Ser201, His241, Glu320, and Phe330, whereas for Gln305, the hydrogen and carbon corresponding to Cβ and Cγ were constrained. For Val203, the carbon and hydrogens that replace its Cα and nitrogen and the carbonyl carbon from the subsequent residue were constrained. In the case of Thr214, Ile216, Asn334, and Ile335, constraints were imposed on the positions of atoms participating in peptide bonds (Figure 4). The Glu190−His191 main chain fragment was modeled with CH_3-NH-CO-CH_3 with constraints imposed on the carbon and hydrogen atoms corresponding to Cα and Cβ. In this way, we usually attempt to keep the integrity of the quantum mechanics (QM) active site model and approximately take into account the rigidity of the protein backbone. Inevitably, this is an approximation and neglects the possibility that the protein's backbone changes its structure along the reaction coordinate. However, in this case, the MD simulation results did not suggest any large movements of the backbone in the vicinity of the active site, at least for the simulated HMS−Fe(IV)═O−HPA species.

The hybrid density functional theory method B3LYP[25,26] was used in quantum chemical studies of the reaction mechanisms. All geometry optimizations were conducted with the double-ζ basis set labeled as lacvp in the Jaguar package. The triple-ζ basis set, combining cc-pVTZ(-f) for C, N, O, and H atoms and lacv3p+ for iron, was used to calculate electronic energies of intermediates and transition states. The solvent corrections were computed using the self-consistent reaction field method.[27,28] The surrounding of the active site model was treated as a macroscopic continuum with a dielectric constant of 4.0, and the solvent accessible surface was determined for a probe radius of 1.4 Å. For all intermediates and transition states, electronic energies computed with the triple-ζ basis set were combined with solvent corrections and were further improved by addition of zero-point and dispersion interaction energies. Such final energies are reported throughout this work, if not stated otherwise. Gaussian 09[29] and Jaguar[30] were used for quantum chemical computations, and figures were produced with VMD.[31] DFT-D2 dispersion corrections for the B3LYP functional were computed with XYZ-Viewer.[19,32] In this study, it was necessary to calculate the minimum energy crossing point (MECP) for potential energy surfaces on which reaction intermediates with different electronic configurations are located. The MECP calculations were performed using a meta-program provided courtesy of J. Harvey.[33] To estimate an energy barrier connected with MECP, geometries of MECP and of the two species that the MECP connects were optimized with a basis set combining lacv3p+ for iron, cc-pVTZ(-f) for N and O atoms directly bound to iron, and lacvp for other atoms. For thus found MECP and its "reactant" and "product", the electronic energy was computed in a full triple-ζ basis set (vide supra) and combined with dispersion and solvation corrections (no ZPE corrections). The value of the MECP barrier was used to construct energy profiles presented here.

RESULTS AND DISCUSSION

Molecular Dynamics Simulations. In the first stage of this study, classical molecular dynamics simulations were performed to model the structure of the HMS−Fe(IV)═O−HPA intermediate, which was then used to construct a large active site model employed in the quantum mechanical investigations.

During the 10 ns long MD simulation, the overall structure of the protein was very well preserved and there were no large structural changes observed in the MD trajectory. The rmsd (atomic root-mean-square displacement), calculated for the protein backbone with respect to the initial (X-ray) structure, reached a plateau at a value of 1.4 Å after dynamics for 7 ns (Figure S1 of the Supporting Information).

Atomic fluctuations calculated with respect to an average structure from the last nanosecond of the simulation demonstrated that the most mobile fragments of the protein are those corresponding to two loops. The first loop, His106−Ala110, includes Glu108, which is missing in the crystal structure. The second mobile loop is in the Asp130−Ala134 fragment. Notably, both loops are located quite far from the active site (Figure S3 of the Supporting Information). Within the active site region, geometry fluctuations are rather subtle

dx.doi.org/10.1021/bi3010957 | *Biochemistry* 2012, 51, 9570−9580

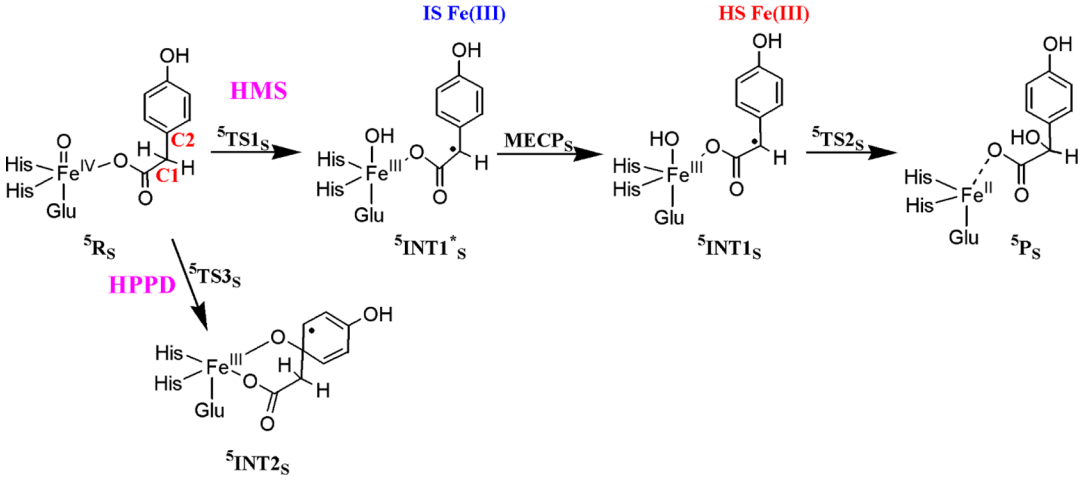

Figure 5. Mechanism of the benzylic hydroxylation catalyzed by HMS and an alternative attack on the aromatic ring, as in the HPPD catalytic cycle.

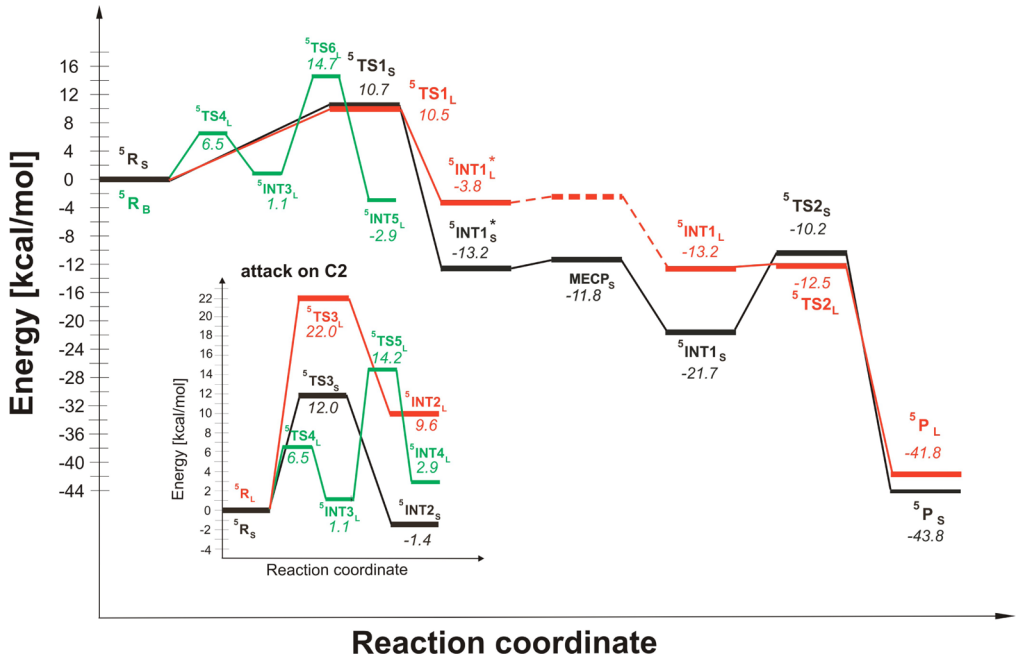

Figure 6. Reaction energy profiles obtained for the small (in black) and large (in orange and green) models. In the inset energy profiles for electrophilic attack on the aromatic ring. The energy of MECP with respect to INT1* does not include ZPE.

and the HPA intermediate shows little mobility inside the substrate pocket. Accordingly, dynamics profiles for distances between the oxo atom (O1) and its three potential reaction partners (see Figure S2 of the Supporting Information), i.e., the *pro-R* and *pro-S* benzylic hydrogens and the aromatic C2 atom, indicate that the *pro-S* hydrogen is in van der Waals contact with the oxo group (average distance of 2.5 Å), whereas the other two atoms are farther away, i.e., at 3.5 Å (C2) and 4.0 Å (*pro-R* H).

In comparison to the active site region in the X-ray structure, only the side chain of Thr214 adopts a different conformation, and it is preserved throughout the 10 ns dynamics (Oγ−Cβ−Cα−C dihedral angle of −170° instead of −50°). To check if this is an artifact caused by trapping the system in a local minimum, additional dynamics simulations were conducted to obtain a potential of mean force (PMF) for the critical dihedral angle of Thr214. The computed PMF (shown in the Supporting Information) indicates that the structure obtained with the MD simulations is a global minimum, and that the conformation corresponding to that observed in the X-ray structure lies around 3 kcal/mol above.

Quantum Chemical Calculations. The benzylic hydroxylation of HPA by HMS was studied previously with DFT methods and minimal active site models involving only the first-shell ligands.[6,7] In the first work,[7] it was found that the cleavage of the benzylic C−H bond of HPA leads to the intermediate-spin Fe(III) species, which is an unusual situation for non-heme iron enzymes.[34] An explanation of this fact was proposed in the second study based on an analysis of symmetry and overlap of frontier molecular orbitals.[6] Thus, the basics of the chemistry performed by HMS are already quite well understood. However, the minimal models cannot explain the origins of the enantio- and regioselectivity of the catalytic reaction. In this study, these unresolved issues were addressed using DFT for two types of active site models. First, a small model was used, and the results obtained are consistent with the previous

dx.doi.org/10.1021/bi3010957 | *Biochemistry* 2012, 51, 9570−9580

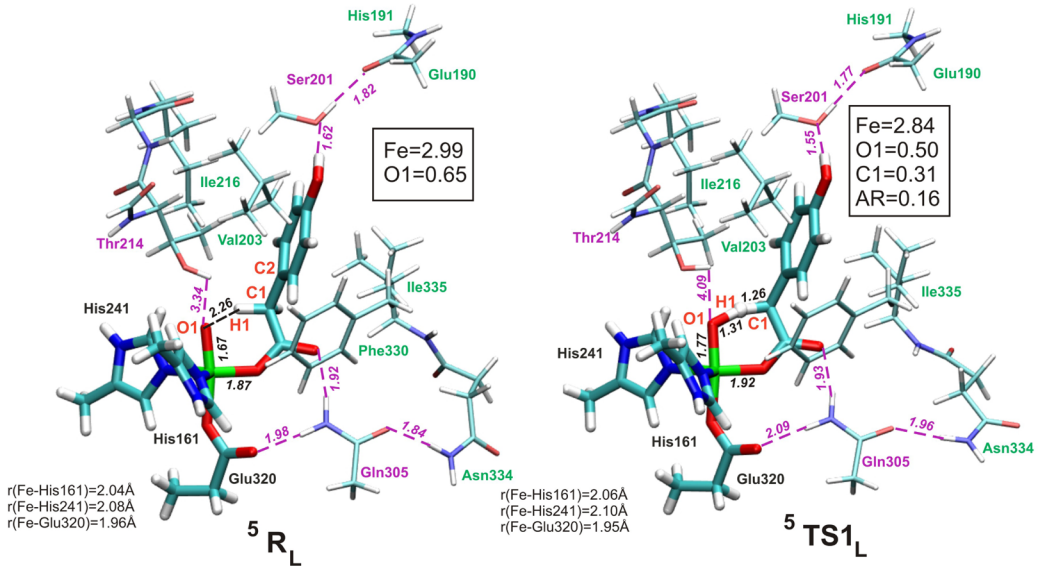

Figure 7. Structures of the oxoferryl intermediate ^5R_L and transition state $^5TS1_L$ found with the large model. In boxes atomic spin populations.

findings, thus serving as a reference for the large model that includes second-shell residues lining the substrate pocket. The results obtained with both models are described in the following subsections.

Small Model. The consensus mechanism for the benzylic hydroxylation catalyzed by HMS is presented in Figure 5, where the alternative electrophilic attack on the aromatic ring, as in the catalytic reaction of HPPD, is also shown.

The HMS reaction proceeds in accord with the rebound mechanism, where in the first step the C−H bond cleavage yields a benzylic radical (^{5}INT1). Subsequent recombination of the organic radical and the Fe(III)-bound OH forms the alcohol product−Fe(II) complex (^{5}P).[7] In the catalytic reaction of HPPD, the reactive Fe(IV)═O group attacks the aromatic ring at C2, which leads to the so-called σ-intermediate (^{5}INT2).

As already mentioned, because of the geometric constraint imposed by direct coordination of the substrate to the metal and the fact that the site of hydroxylation neighbors the carboxylic group bound to iron, the activation of the C−H bond engages a π^* orbital of the Fe(IV)═O group instead of the σ^* orbital usually involved, and as a consequence, it leads to a radical intermediate featuring the intermediate-spin Fe(III) (^{5}INT1*) coupled ferromagnetically with the benzylic radical.[6] This is an excited state that in the subsequent step is de-excited by an internal conversion to the electronic ground state with a high-spin configuration on Fe(III) and antiferromagnetic coupling to the benzylic radical. The reaction energy profiles are presented in Figure 6.

The lowest-energy path for the benzylic hydroxylation involves a barrier of 10.7 kcal/mol connected with the C−H bond cleavage ($^5TS1_S$), which can be compared with the previously computed values of 14.0 kcal/mol[6] and 15.4 kcal/mol[7] (here corrected with our ZPE and vdW corrections). The potential energy surface (PES) of the resulting IS Fe(III) species ^{5}INT1* crosses with PES of the HS ground state with the minimal energy crossing point (MECP) located very near the equilibrium geometry of the excited state (only 1.4 kcal/mol higher). Thus, the internal conversion involves a negligible barrier connected with the MECP, and it leads to a decrease in energy by 8.4 kcal/mol, which can be compared to the value of 7.3 kcal/mol obtained in the previous study.[7] The final step on the lowest-energy path is the OH rebound, which involves a barrier of 11.5 kcal/mol ($^5TS2_S$) and leads to the benzylic alcohol product (^5P_S). It is worth noting that in the previous study a significantly lower barrier for OH rebound was found (6.7 kcal/mol). This discrepancy has its origin in different geometries obtained for $^5INT1_S$ in the two studies. In the study presented here, a hydrogen bond between the Fe-bound OH and the carboxylic group of HPA is present in the $^5INT1_S$ intermediate, which both stabilizes $^5INT1_S$ and increases the barrier for OH rebound, as this H-bond has to be broken to reach the TS2 geometry. The energy of the overall hydroxylation reaction computed with the small model is −43.8 kcal/mol, which agrees reasonably well with the value of −39.0 kcal/mol obtained in the previous study.[7]

As expected, with the small model, the selectivity between the reaction channels leading to the *S*- and *R*-alcohol products is not described well. The barrier connected with hydroxylation leading to the *R*-alcohol is found to be slightly lower, by 1.6 kcal/mol, than for the channel yielding the *S*-alcohol.

Besides the lowest-energy mechanism summarized above, two alternatives not tested previously and proceeding on the low-lying excited potential energy surfaces were considered here. However, these reaction paths were found to be rather unlikely, and they are described in the Supporting Information.

In the catalytic cycle of HPPD, the oxoferryl species attacks the aromatic ring at the carbon substituted with the carboxymethyl side chain (C2), which is a reaction competitive to the benzylic hydroxylation at C1. Because C2 is separated from iron by one more covalent bond than C1, it can approach the oxoferryl species with a wider Fe−O−C angle, and this allows the usual Fe−O σ^* orbital to be involved in the reaction. This type of electrophilic attack on the aromatic ring is connected with a barrier of 12.0 kcal/mol ($^5TS3_S$), which is only 1.3 kcal/mol larger than the barrier to C−H bond cleavage. Interestingly, for the attack on C2, it was possible to locate the second reaction channel, i.e., the one involving the Fe−O π^* orbital. This reaction proceeds through $^5TS3_S^*$ with an activation energy of 16.9 kcal/mol (almost 5 kcal/mol above $^5TS3_S$) and leads to $^5INT2_S^*$ featuring IS Fe(III).

Large Model. Benzylic Hydroxylation. The structure of the HMS−Fe(IV)═O−HPA intermediate optimized with the

dx.doi.org/10.1021/bi3010957 | *Biochemistry* 2012, 51, 9570−9580

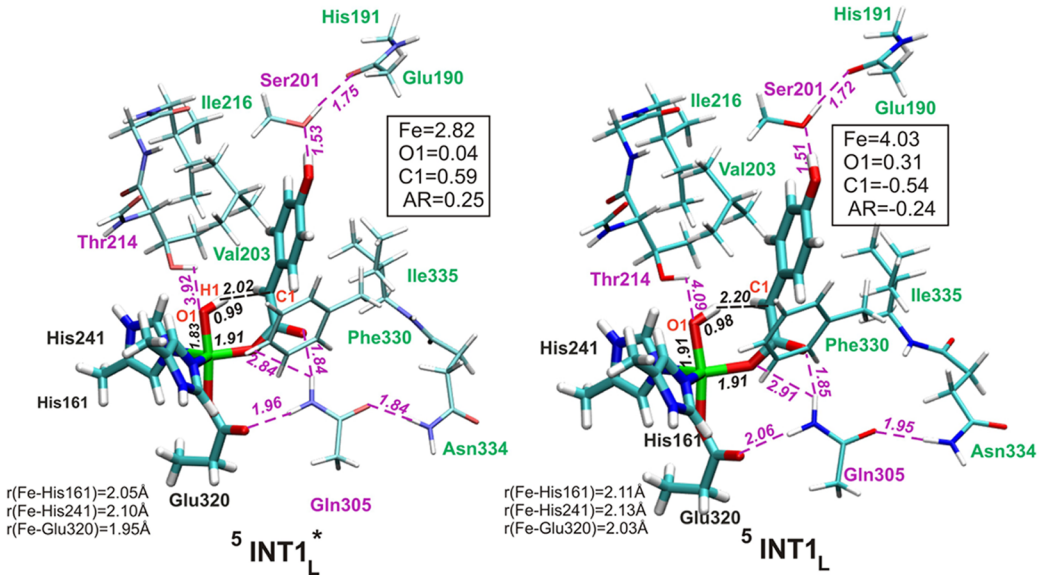

Figure 8. Structures of the IS Fe(III) intermediate ^{5}INT1$_L^*$ and HS Fe(III) intermediate ^{5}INT1$_L$ found with the large model. In boxes atomic spin populations.

large model, i.e., ^{5}R$_L$, is consistent with the macromolecular model obtained with MD simulations, and it confirms that the active site of HMS is ideally shaped to keep the *pro-S* benzylic hydrogen close to the oxo ligand (Figure 7). Indeed, in ^{5}R$_L$, the O1−H1 distance equals only 2.26 Å (2.5 Å in MD) and the C−H bond vector roughly points along the O−C vector, both factors favoring C−H bond cleavage. On the other hand, the distance between the *pro-R* benzylic hydrogen and the oxo ligand amounts to 3.92 Å and the hypothetical abstraction of the *pro-R* hydrogen would require substantial rearrangement of second-shell residues. Indeed, a PMF profile computed for shortening the distance between the *pro-R* benzylic hydrogen and the oxo ligand, in the range of 2.00−4.00 Å, revealed that bringing the *pro-R* hydrogen to within 2.50 Å of the oxo ligand requires the investment of 6 kcal/mol. These structural and energetic results explain the stereospecificity of the HMS catalytic reaction.

With regard to hydrogen bonding interactions in ^{5}R$_L$, Ser201 participates in two hydrogen bonds: with the hydroxyl group of HPA (1.62 Å) and with the oxygen from the Glu190−His191 peptide bond (1.82 Å). Another residue important for anchoring HPA in the active site is Glu305, which forms hydrogen bonds with the carboxyl oxygen atoms of HPA and Glu320 and the side chain of Asn334. Thr214 participates in a stretched H-bond with the oxo group. All these H-bonds are present in the HMS−Co(II)−HMA crystal structure (PDB entry 2R5V).

In the transition state for the benzylic hydrogen atom abstraction for the ground state Fe(IV)═O species (^{5}TS1$_L$), the Fe−O1 and C1−H1 distances are 1.77 and 1.26 Å, respectively, whereas the O1−H1 distance is 1.31 Å (Figure 7). In TS1 obtained with the small model (^{5}TS1$_S$), these distances are very similar, i.e., 1.78, 1.27, and 1.29 Å, respectively. Thus, within the active site of HMS, the geometry of TS1 is very similar to that obtained in a vacuum (with no constrains imposed on the model). In parallel, the activation energies for the C−H bond cleavage calculated with the small and large models are very similar, i.e., 10.5 and 10.7 kcal/mol, respectively (Figure 6). Comparing the hydrogen bond lengths in the structures of ^{5}TS1$_L$ and ^{5}R$_L$, we can notice that the H-bonds formed by Ser201 are noticeably shorter in the transition state structure (1.55 and 1.77 Å compared to 1.62 and 1.82 Å, respectively). On the other hand, two of three H-bonds formed by Glu305 are elongated in the TS.

With the use of the substrate dideuterated at the benzylic carbon, the kinetic isotope effect (KIE) was measured for benzylic hydroxylation by two HMS mutants, i.e., I216N and S201A, and KIE amounted to 2.2 and 2.6, respectively.[8] The value computed in this work with the large model for WT HMS amounts to 5.88 (7.84 with the Wigner correction for tunneling).

From ^{5}TS1$_L$, ^{5}INT1$_L^*$ with IS Fe(III) and a benzylic radical is reached (Figure 8) and the energy of this reaction computed with the large model is −3.8 kcal/mol; for the small model, it amounts to −13.2 kcal/mol. This discrepancy has its origin in the conformational freedom of the substrate in the small model, where it rotates along the Fe−O bond and forms an H-bond with the Fe(III)-bound OH group. Obviously, in the large model, this type of rotation of the substrate is hindered by the presence of the second-shell residues.

Like for the small model, an intersystem crossing connected with a change in the electronic configuration on Fe(III) from intermediate-spin to high-spin and a change in spin coupling to the benzylic radical from ferromagnetic to antiferromagnetic (^{5}INT1$_L^*$ → ^{5}INT1$_L$) lowers the potential energy of the system by 9.4 kcal/mol (in the small model by 8.5 kcal/mol). The barrier connected with MECP is assumed to be the same as for the small model. This fragment of the energy profile is shown as the dashed line in Figure 6.

For ^{5}INT1$_L$, the hydrogen bonding interactions provided by Ser201 with the HPA hydroxyl group (1.51 Å) and Ser201 with the oxygen of the Glu190−His191 peptide bond (1.72 Å) are shorter than for ^{5}R$_L$ by 0.09 and 0.1 Å, respectively. The Glu305−HPA carboxylate H-bond is shortened from 1.92 to 1.85 Å, whereas the two other H-bonds formed by Glu305 are elongated from 1.98 to 2.06 Å (H-bond to Glu320) and from 1.84 to 1.95 Å (H-bond to Asn334). The change in the electronic configuration on iron is accompanied by elongation of the coordination bonds, with the exception for the Fe−substrate bond that is not affected (Figure 8).

dx.doi.org/10.1021/bi3010957 | *Biochemistry* 2012, 51, 9570−9580

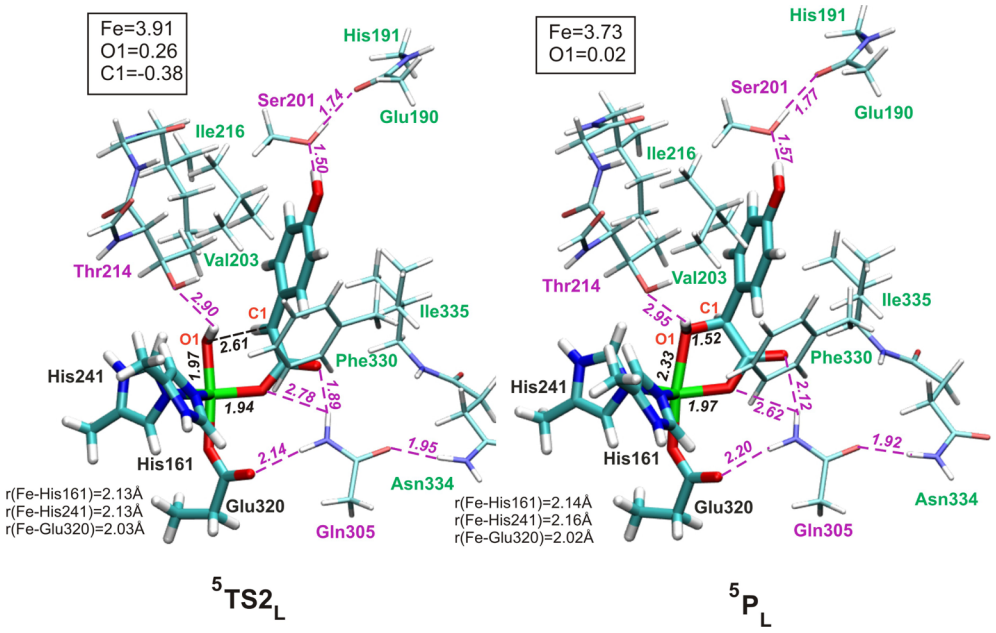

Figure 9. Structures of transition state ^{5}TS2$_L$ and product complex ^{5}P$_L$ found with the large model. In boxes atomic spin populations.

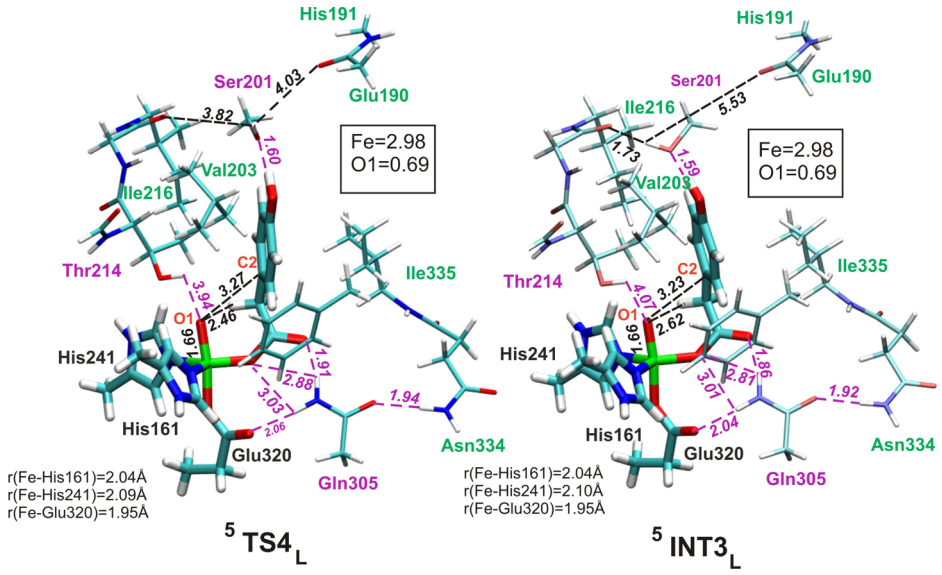

Figure 10. Structures of transition state ^{5}TS4$_L$ for Ser201 rotation and oxoferryl intermediate ^{5}INT3$_L$ with Ser201 rotated, found with the large model. In boxes atomic spin populations.

The OH rebound step on the ground state PES of the large model proceeds through ^{5}TS2$_L$, which is shown in Figure 9 together with the product complex (^{5}P$_L$). Compared to ^{5}INT1$_L$ (Figure 8), in ^{5}TS2$_L$ the OH ligand is rotated (along the Fe−O axis) so that its oxygen can develop a bond with the benzylic carbon. This relatively minor structural change, accompanied by a slight elongation of the Fe−O bond (from 1.91 to 1.97 Å) and shortening of the O−C distance (from 3.06 to 2.61 Å), is connected with a very small activation barrier of 0.7 kcal/mol. The height of this barrier is lower than the expected accuracy of the current model and method, so it is not unprobable that in reality there is no barrier connected with this step. The structure of ^{5}P$_L$ can be directly compared with the active site region of the HMS−Co(II)−HMA X-ray structure (PDB entry 2R5V), as it corresponds to the same stage of the catalytic reaction, with the minor difference connected with the metal substitution. Superimposed structures of ^{5}P$_L$ and the active site region of PDB entry 2R5V agree quite well (Figure S10 of the Supporting Information), with some displacements on the Thr214−Ile216 and Glu190−His191 fragments and a conformational change in the side chain of Thr214 (vide supra).

The reaction energy profiles for benzylic hydroxylation obtained with the small and large models (Figure 6) agree very well with the exception of the ^{5}INT1*−^{5}INT1 part of the PES, where the "intruder" H-bond between the Fe-bound OH and the carboxylic group of the substrate forms in the small model. This agreement suggests that the active site of HMS is shaped in such a way that benzylic hydroxylation can proceed with no unfavorable steric interactions that would increase the barrier. This is in contrast to the electrophilic attack on the ring, which is covered in the next subsection.

dx.doi.org/10.1021/bi3010957 | *Biochemistry* 2012, 51, 9570−9580

Electrophilic Attack on the Aromatic Ring. The computational results obtained for the small model (vide supra) indicate that there is a very small intrinsic difference in activation energies for C−H bond cleavage (10.7 kcal/mol) and the electrophilic attack on the ring (12.0 kcal/mol). Therefore, it was interesting to characterize the reaction channel for the electrophilic attack with the large model to identify the structural features of the HMS active site responsible for the reaction specificity. Interestingly, two variants of the electrophilic attack reaction that differ in the conformation of Ser201 were found.

Direct attack of the oxo group on C2 proceeds through ^{5}TS3$_L$ (Figure S7 of the Supporting Information), which is connected with a surprisingly high activation barrier of 22 kcal/mol (inset of Figure 6) and leads to a cationic σ-complex ^{5}INT2$_L$ with a computed energy of 9.6 kcal/mol. The two major factors that cause this large activation energy are the suboptimal H-bond distance between Ser201 and the Glu190−His191 backbone and the large pyramidylization of C2. Compared to that in ^{5}R$_L$, in ^{5}TS3$_L$ the H-bond stretches from 1.82 to 2.05 Å, whereas the improper dihedral angle at C2 is −145° (−155° in ^{5}TS3$_S$). Thus, in HMS, the lowest-energy conformation of the active site strongly disfavors the electrophilic attack on the ring.

In the known structures of HPPD, Ser201 adopts a conformation different from that observed in HMS. More specifically, the backbone fragment corresponding to the Glu190−His191 fragment in HMS is shifted farther from Ser201. As a result, Ser201 forms an H-bond with the backbone oxygen of a residue corresponding to Ile216 in HMS. Motivated by these structural differences between HMS and HPPD, we checked if Ser201 could adopt this second conformation in HMS and what bearing it would have on the reaction barriers. The transition state for rotation of the Ser201 side chain [^{5}TS4$_L$ (Figure 10)] was located 6.5 kcal/mol above ^{5}R$_L$ (Figure 6), leading to a second conformation of the oxoferryl species intermediate, ^{5}INT3$_L$.

A comparison of the structures of ^{5}R$_L$ (Figure 7) and ^{5}INT3$_L$ (Figure 10) reveals that the flip of the Ser201 side chain affects the distances critical for reaction specificity. Indeed, the oxo−*pro-S* hydrogen distance is increased from 2.26 to 2.62 Å, whereas the oxo−C2 distance is shortened from 3.61 to 3.23 Å. Most importantly, these geometric changes translate to a lowering of the activation barrier for the attack on the ring by 7.8 kcal/mol. The energy of ^{5}TS5$_L$ (Figure S8 of the Supporting Information) is 14.2 kcal/mol (inset in Figure 6). An analysis of the structure of ^{5}TS5$_L$ shows that once the side chain of Ser201 is rotated, the attack on C2 can proceed while maintaining an optimal H-bond distance between Ser201 and Ile216 and pyramidylizaton at C2 (−151°) that is close to optimal (−155°).

The large model employed in this study successfully reproduces the regioselectivity of HMS. The activation barrier for the electrophilic attack on the ring via ^{5}TS5$_L$ (14.2 kcal/mol) is 3.7 kcal/mol higher than the barrier for the native reaction of HMS, i.e., benzylic hydroxylation. This means that the intrinsic difference of 1.3 kcal/mol between the barriers is enhanced by 2.4 kcal/mol in the active site of HMS. In an attempt to estimate the individual contributions of the second-shell residues to this enhancement, we calculated, using the Amber force field, the nonbonded (van der Waals and electrostatics) interactions of atoms from the second-shell residues for the two transition states and reactant ^{5}R$_L$. The differences calculated with respect to ^{5}R$_L$ show how much the nonbonded interactions of a given atom are (de)stabilizing a given transition state, and their gross values for the side chains of the second-shell residues are listed in Table 1. An analysis of these values reveals that the leading residues destabilizing ^{5}TS5$_L$ with respect to ^{5}TS1$_L$ are Phe330 (+1.07 kcal/mol), Ile335 (+0.99 kcal/mol), and Thr214 (+0.72 kcal/mol), of which Thr214 and Ile335 are strictly conserved in HMS. Their counterparts in HPPD are Pro214 and Phe337. The methyl group of the Thr214 side chain hinders the approach of the aromatic ring to the oxo ligand in ^{5}TS5$_L$ (two close contacts of ∼3.3 Å with aromatic carbons of HPA), whereas Ile335 interacts with the HPA aromatic ring less efficiently because of the tilt of the ring caused by the rotation of the Ser201 side chain. Notably, these differences in the side chain contributions sum to +1.46 kcal/mol, which corresponds to ∼61% of the 2.4 kcal/mol barrier enhancement caused by the second-shell residues (included in the current large model).

Table 1. Relative (with respect to ^{5}R$_L$) Gross Nonbonded Contributions (in kilocalories per mole) to the Activation Energies by the Side Chains of the Second-Shell Residues

residue	^{5}TS1$_L$	^{5}TS5$_L$
Ser201	+0.16	−0.94
Val203	+0.64	+0.85
Thr214	+1.65	+2.37
Ile216	+0.20	+0.60
Gln305	+0.29	+0.16
Phe330	−0.03	+1.04
Asn334	+0.91	+0.20
Ile335	−0.50	+0.49

Interestingly, the conformation of Ser201 was found to play a key role in determining the reaction regioselectivity. More specifically, for the large model with Ser201 rotated (^{5}INT3$_L$), a transition state for benzylic hydrogen atom abstraction was found (^{5}TS6$_L$, 14.7 kcal/mol), and it lies 0.5 kcal/mol above ^{5}TS5$_L$, which is a TS for electrophilic attack on the aromatic ring. In other words, different reaction channels are preferred for the two conformations of Ser201: cleavage of the benzylic C−H bond and electrophilic attack on the ring. Moreover, the conformation of Ser201, and by extension possibly its presence and/or ability to form a H-bond with the phenolic OH group of the substrate, is more vital for the attack on the ring than for C−H bond cleavage.[35] Indeed, the flip of the Ser201 side chain causes the barrier to C−H bond cleavage to increase by 3.7 kcal/mol, whereas the barrier to the attack on the ring decreases by more than twice this quantity, i.e., by 7.8 kcal/mol. This different "sensibility" of the two reactions to structural details of Ser201 would be in line with the finding that a HMS S201A mutant produces considerably less (12%) HPA, which is a shunt product, than an analogous HPPD S230A construct (30.6%).[8]

CONCLUSIONS

The results of this study have improved the understanding of the mechanism of benzylic hydroxylation catalyzed by HMS. First, the unusual mechanism of C−H bond cleavage leading to the intermediate-spin Fe(III) species[6,7] was confirmed by ruling out the alternative, where the excited state of the oxoferryl species is involved. Similarly, the OH rebound step was shown

dx.doi.org/10.1021/bi3010957 | *Biochemistry* 2012, 51, 9570−9580

to proceed on the ground state PES, because the internal conversion (via MECP) involves a significantly lower barrier than the OH rebound on the excited state PES (Figure S5 of the Supporting Information). Second, molecular dynamics simulations for the HMS−Fe(IV)═O−HPA intermediate confirmed the conclusions concerning the reaction regioselectivity, formulated on the basis of the X-ray structure and dynamics simulations for the HMS−Fe(II)−HPP complex.[5] In the 10 ns long dynamics trajectory, the *pro-S* benzylic hydrogen remains in van der Waals contact with the oxo ligand, whereas the *pro-R* hydrogen and aromatic C2 are kept farther away (Figure S2 of the Supporting Information). Moreover, a comparison of the reaction profiles obtained with the small and large models showed that the HMS active site is optimally shaped to catalyze the benzylic hydroxylation reaction (Figure 6). An investigation of the alternative reaction, i.e., electrophilic attack on the aromatic ring of HPA, provided some interesting insights into the role played by the second-shell residues in directing the catalytic reaction. Most notably, the conformation of the Ser201 side chain modulates, through its H-bond with the phenyl group of HPA, the orientation of HPA in the active site. When Ser201 H-bonds to the Glu190−His191 backbone oxygen, the *pro-S* hydrogen is exposed to the oxo group; when Ser201 interacts with the Leu215−Ile216 backbone oxygen, aromatic C2 comes closer to the oxo ligand and the barrier to the attack on the ring decreases from 22.0 to 14.2 kcal/mol (inset in Figure 6). An analysis of the nonbonded interactions for the oxoferryl intermediate and transition states for C−H bond cleavage and electrophilic attack on the ring revealed that within the HMS active site the attack on the ring is prevented mainly by Thr214, Phe330, and Ile335 (Table 1). This type of catalytic strategy, where the substrate is positioned so that only one part of it can interact with the reactive intermediate and the approach of the other parts is hindered by steric interactions, is known as negative catalysis,[36] which is commonly realized by metalloenzymes producing reactive species in their catalytic cycles.[37] The ongoing studies of the reaction mechanism of HPPD should complement these findings and help in obtaining a full picture of the strategies employed by Nature to control the reactivity of the oxoferryl species produced by these two closely related dioxygenases.

■ ASSOCIATED CONTENT

Supporting Information

The rmsd's for backbone atoms during 10 ns long dynamics (Figure S1), dynamics profiles for distances critical for reaction specificity (Figure S2), mobile loops of HMS (Figure S3), PMF profile for the rotation of the Thr214 side chain (Figure S4), reaction energy profiles obtained with the small model (Figure S5), contours of α-LUMO orbitals for $^5R_S^*$ and $^5TS1_S^*$ (Figure S6), structures of transition state $^5TS3_L$ and HS Fe(II) intermediate $^5INT2_L$ (Figure S7), structures of transition state $^5TS5_L$ and high-spin Fe(II) intermediate $^5INT4_L$ (Figure S8), structures of transition states $^5TS6_L$ and $^5INT5_L^*$ (Figure S9), superimposed structures of optimized product complex ^5P_L and the active site region of the crystal structure of PDB entry 2R5V (Figure S10), the very small model used in DFT and CCSD(T) calculations (Figure S11), a short discussion of reaction paths involving low-lying excited states, the computational details and extrapolation procedure used to estimate the energy of $^5R^*$ based on CCSD(T) results, Cartesian coordinates and calculated energies for all structures, and a PDB file with the whole protein model minimized after 10 ns long dynamics. This material is available free of charge via the Internet at http://pubs.acs.org.

■ AUTHOR INFORMATION

Corresponding Author

*Jerzy Haber Institute of Catalysis and Surface Chemistry, Polish Academy of Sciences, ul. Niezapominajek 8, 30-239 Cracow, Poland. Telephone: +48 12 6395158. Fax: +48 12 4251923. E-mail: ncborows@cyf-kr.edu.pl.

Funding

This research project was part of "Kraków Interdisciplinary PhD-Project in Nanoscience and Advanced Nanostructures" operated within the Foundation for Polish Science MPD Programme cofinanced by the EU European Regional Development Fund. The project was supported by Grants DEC-2011/01/N/ST4/02330 and UMO-2011/01/B/ST4/02620 from the National Science Centre, Poland.

Notes

The authors declare no competing financial interest.

■ ACKNOWLEDGMENTS

We are grateful to Prof. Jeremy Harvey and Sven de Marothy for providing us with Crossing and XYZ-Viewer, respectively.

■ REFERENCES

(1) Choroba, O., Williams, D., and Spencer, J. (2000) Biosynthesis of the vancomycin group of antibiotics: Involvement of an unusual dioxygenase in the pathway to S-4-hydroxyphenylglycine. *J. Am. Chem. Soc. 122*, 5389−5390.

(2) Knox, W. E., and Edwards, S. (1955) Enzymes involved in conversion of tyrosine to acetoacetate. *Methods Enzymol. 2*, 287−300.

(3) He, P., and Moran, G. (2011) Structural and mechanistic comparisons of the metalbinding members of the vicinal oxygen chelate (voc) superfamily. *J. Inorg. Biochem. 105*, 1259−1272.

(4) Moran, G. R. (2005) 4-Hydroxyphenylpyruvate dioxygenase. *Arch. Biochem. Biophys. 433*, 117−128.

(5) Brownlee, J., He, P., Moran, G. R., and Harrisson, D. H. T. (2008) Two roads diverged: The structure of hydroxymandelate synthase from *Amycolatopsis orientalis* in complex with 4-hydroxymandelate. *Biochemistry 47*, 2002−2013.

(6) Neidig, M., Decker, A., Choroba, O., Huang, F., Kavana, M., Moran, G., Spencer, J., and Solomon, E. (2006) Spectroscopic and electronic structure studies of aromatic electrophilic attack and hydrogen-atom abstraction by non-heme iron enzymes. *Proc. Natl. Acad. Sci. U.S.A. 103*, 12966−12973.

(7) Borowski, T., Bassan, A., and Siegbahn, P. E. M. (2004) 4-Hydroxyphenylpyruvate dioxygenase: A hybrid density functional study of the catalytic reaction mechanism. *Biochemistry 43*, 12331−12342.

(8) Shah, D. D., Conrad, J. A., Heinz, B., Brownlee, J. M., and Moran, G. R. (2011) Evidence for the mechanism of hydroxylation by 4-hydroxyphenylpyruvate dioxygenase and hydroxymandelate synthase from intermediate partitioning in active site variants. *Biochemistry 50*, 7694−7704.

(9) Krebs, C., Galonić Fujimori, D., Walsh, C. T., and Bollinger, J. M., Jr. (2007) Non-heme Fe(IV)-oxo intermediates. *Acc. Chem. Res. 40*, 484−492.

(10) Gunsior, M., Ravel, J., Challis, G. L., and Townsend, C. A. (2004) Engineering phydroxyphenylpyruvate dioxygenase to a p-hydroxymandelate synthase and evidence for the proposed benzene oxide intermediate in homogentisate formation. *Biochemistry 43*, 663−674.

(11) O'Hare, H., Huang, F., Holding, A., Choroba, O., and Spencer, J. (2006) Conversion of hydroxyphenylpyruvate dioxygenases into hydroxymandelate synthases by directed evolution. *FEBS Lett. 580*, 3445−3450.

(12) Eswar, N., Marti-Renom, M., Webb, B., Madhusudhan, M., Eramian, D., Shen, M., Pieper, U., and Sali, A. (2006) Comparative protein structure modeling with modeller. In *Current Protocols in Bioinformatics*, Supplement 15, pp 5.6.1−5.6.30, John Wiley and Sons, Inc., New York.
(13) Marti-Renom, M., Stuart, A., Fiser, A., Sánchez, R., Melo, F., and Sali, A. (2000) Comparative protein structure modeling of genes and genomes. *Annu. Rev. Biophys. Biomol. Struct. 29*, 291−325.
(14) Sali, A., and Blundell, T. (1993) Comparative protein modelling by satisfaction of spatial restraints. *J. Mol. Biol. 234*, 779−815.
(15) Fiser, A., Do, R. K., and Sali, A. (2000) Modeling of loops in protein structures. *Protein Sci. 9*, 1753−1773.
(16) Li, H., Robertson, A., and Jensen, J. (2005) Very fast empirical prediction and rationalization of protein pKa values. *Proteins 61*, 704−721.
(17) Bas, D., Rogers, D., and Jensen, J. (2008) Very fast prediction and rationalization of pKa values for protein-ligand complexes. *Proteins 73*, 765−783.
(18) Seminario, J. M. (1996) Calculation of intramolecular force fields from second derivative tensors. *Int. J. Quantum Chem., Quantum. Chem. Symp. 30*, 1271−1277.
(19) de Marothy, S. (2009) *XYZ-Viewer*, version 0.965 (http://www.physto.se/sven/).
(20) Wang, J., Cieplak, P., and Kollman, P. A. (2000) How well does a restrained electrostatic potential (RESP) model perform in calculating conformational energies of organic and biological molecules. *J. Comput. Chem. 21*, 1049−1074.
(21) Rappe, A., Casewit, C., Colwell, K., Goddard, W., and Skiff, W. (1992) Uff, a full periodic table force field for molecular mechanics and molecular dynamics simulations. *J. Am. Chem. Soc. 114*, 10024−10035.
(22) Duan, Y., Wu, C., Chowdhury, S., Lee, M. C., Xiong, G., Zhang, W., Yang, R., Cieplak, P., Luo, R., Lee, T., Caldwell, J., Wang, J., and Kollman, P. (2003) A point-charge force field for molecular mechanics simulations of proteins based on condensed-phase quantum mechanical calculations. *J. Comput. Chem. 24*, 1999−2012.
(23) Jorgensen, W. L., Chandrasekhar, J., Madura, J. D., Impey, R. W., and Klein, M. L. (1983) Comparison of simple potential functions for simulating liquid water. *J. Chem. Phys. 79*, 926−935.
(24) Case, D., Darden, T., Cheatham, T., III, Simmerling, C., Wang, J., Duke, R., Luo, R., Walker, R., Zhang, W., Merz, K., Roberts, B., Wang, B., Hayik, S., Roitberg, A., Seabra, G., Kolossváry, I., Wong, K., Paesani, F., Vanicek, J., Wu, X., Brozell, S., Steinbrecher, T., Gohlke, H., Cai, Q., Ye, X., Wang, J., Hsieh, M.-J., Cui, G., Roe, D., Mathews, D., Seetin, M., Sagui, C., Babin, V., Luchko, T., Gusarov, S., Kovalenko, A., and Kollman, P. (2010) *AMBER11*, University of California, San Francisco.
(25) Becke, A. D. J. (1993) Density-functional thermochemistry. III. The role of exact exchange. *Chem. Phys. 98*, 5648−5652.
(26) Lee, C., Yang, W., and Parr, R. G. (1988) Development of the Colle-Salvetti correlation energy formula into a functional of the electron density. *Phys. Rev. B37*, 785−789.
(27) Tannor, D. J., Marten, B., Murphy, R., Friesner, R. A., Sitkoff, D., Nicholls, A., Ringnalda, M., Goddard, W. A., III, and Honig, B. (1994) Accurate first principles calculation of molecular charge distributions and solvation energies from ab initio quantum mechanics and continuum dielectric theory. *J. Am. Chem. Soc. 116*, 11875−11882.
(28) Marten, B., Kim, K., Cortis, C., Friesner, R. A., Murphy, R., Ringnalda, M., Sitkoff, D., and Honig, B. (1996) New model for calculation of solvation free energies: Correction of self-consistent reaction field continuum dielelectric theory for short-range hydrogen-bonding effects. *J. Phys. Chem. 100*, 11775−11788.
(29) Frisch, M., Trucks, G., Schlegel, H., Scuseria, G., Robb, M., Cheeseman, J., Scalmani, G., Barone, V., Mennucci, B., Petersson, G., Nakatsuji, H., Caricato, M., Li, X., Hratchian, H., Izmaylov, A., Bloino, J., Zheng, G., Sonnenberg, J., Hada, M., Ehara, M., Toyota, K., Fukuda, R., Hasegawa, J., Ishida, M., Nakajima, T., Honda, Y., Kitao, O., Nakai, H., Vreven, T., Montgomery, J., Jr., Peralta, J., Ogliaro, F., Bearpark, M., Heyd, J., Brothers, E., Kudin, K., Staroverov, V., Kobayashi, R., Normand, J., Raghavachari, K., Rendell, A., Burant, J., Iyengar, S., Tomasi, J., Cossi, M., Rega, N., Millam, J. M., Klene, M., Knox, J., Cross, J., Bakken, V., Adamo, C., Jaramillo, J., Gomperts, R., Stratmann, R., Yazyev, O., Austin, A. J., Cammi, R., Pomelli, C., Ochterski, J., Martin, R., Morokuma, K., Zakrzewski, V., Voth, G., Salvador, P., Dannenberg, J., Dapprich, S., Daniels, A., Farkas, Ö., Foresman, J., Ortiz, J., Cioslowski, J., and Fox, D. (2009) *Gaussian 09*, revision A.1, Gaussian Inc., Wallingford, CT.
(30) *JAGUAR 7.6* (2009) Schrödinger, Inc., Portland, OR.
(31) Humphrey, W., Dalke, A., and Schulten, K. (1996) VMD: Visual Molecular Dynamics. *J. Mol. Graphics 14*, 33−38.
(32) Grimme, S. (2006) Semiempirical gga-type density functional constructed with a longrange dispersion correction. *J. Comput. Chem. 27*, 1787−1799.
(33) Harvey, J. N., Aschi, M., Schwarz, H., and Koch, W. (1998) The singlet and triplet states of phenyl cation. A hybrid approach for locating minimum energy crossing points between non-interacting potential energy surfaces. *Theor. Chem. Acc. 99*, 95−99.
(34) Bassan, A., Blomberg, M. R., Borowski, T., and Siegbahn, P. E. (2006) Theoretical studies of enzyme mechanisms involving high-valent iron intermediates. *J. Inorg. Biochem. 100*, 727−743.
(35) Baldwin, J. E., Crouch, N. P., Fujishima, Y., Lee, M. H., MacKinnon, C. H., Pitt, J. P. N., and Willis, A. C. (1995) 4-Hydroxyphenylpyruvate dioxygenase appears to display α-ketoisocaproate dioxygenase activity in rat liver. *Bioorg. Med. Chem. Lett. 5*, 1255−1260.
(36) Rétey, J. (1990) Enzymic reaction selectivity by negative catalysis or how do enzymes deal with highly reactive intermediates? *Angew. Chem., Int. Ed. 29*, 355−361.
(37) Borowski, T., and Siegbahn, P. (2011) *Iron-Containing Enzymes. Versatile Catalysts of Hydroxylation Reactions in Nature* (de Visser, S. P., and Kumar, D., Eds.) pp 88−118, Royal Chemistry Society Publishing, Cambridge, U.K.